Interfacial Stresses in Single-Side Composite Patch-Repairs with Material Tailored Bondline

M. A. Khan[a], S. Kumar[a,1]

[a]*Institute Center for Energy (iEnergy),*

Department of Mechanical and Materials Engineering,

Masdar Institute of Science and Technology,

PO Box 54224, Abu Dhabi, UAE

Abstract

A stress-function approach to investigate the stress-state in an adhesively bonded single-side composite patch-repair system containing a through-thickness hairline defect in the substrate experiencing far-field tensile stresses is presented. Results obtained indicate that the peak adhesive stresses can be significantly minimized and they can be more uniformly distributed over the bondlength employing a material tailored bondline in lieu of a homogeneous bondline. The proposed model can be used as a simple and efficient analytical tool for designing such composite crack-patch systems and to examine the effect of loss of interface stiffness due to an existing defect and/or damage in the bondline.

Interfacial stresses, variational method, patch-repair, material tailoring, composites, adhesives

[1]Corresponding author: s.kumar@eng.oxon.org, skumaar@mit.edu,
Tel.:+971 2 810 9239, Fax: +971 2 698 8121

Nomenclature

σ_0	Far-field stress in the substrate
h_i	Thickness of the member $'i'$
a	Radius of axisymmetric substrate-adhesive-patch system
b, c, d	Geometric parameters $b = h_1,\ c = b + h_3$, and $d = c + h_2$
δr	Radius of hairline crack
$E_r^{(i)}, E_\theta^{(i)}, E_z^{(i)}$	Young's modulus of the transversely isotropic member $'i'$ in r, θ and z directions respectively
$E^{(i)}, \nu^{(i)}, G^{(i)}$	Young's modulus, Poisson's ratio and shear modulus of an isotropic member $'i'$ respectively
$E^{(i)}(r), G^{(i)}(r)$	Young's modulus and shear modulus of an graded adhesive respectively
$\nu_{rz}^{(1)}, \nu_{r\theta}^{(1)}$	Poisson's ratio of the substrate
$\nu_{rz}^{(2)}, \nu_{r\theta}^{(2)}$	Poisson's ratio of repair-patch
$\nu_{rz}^{(3)}, \nu_{r\theta}^{(3)}$	Poisson's ratio of adhesive interlayer
$G_{rz}^{(1)}$	Shear modulus of the substrate along $r - z$ direction
$G_{rz}^{(2)}$	Shear modulus of the patch along $r - z$ direction
$\alpha_r^{(i)}, \alpha_\theta^{(i)}, \alpha_z^{(i)}$	Coefficient of thermal expansion in r, θ and z directions respectively
ΔT	Uniform temperature change from stress-free-state
$K_1^{(1)}, K_2^{(1)}, K_1^{(2)}$ $K_2^{(2)}, K_1^{(3)}, K_2^{(3)}$	Constants of integration needed to satisfy the boundary conditions
$U_d^{(1)}, U_d^{(2)}, U_d^{(3)}$	Strain energy density in the substrate, patch and adhesive respectively
$U^{(1)}, U^{(2)}, U^{(3)}$	Complementary strain energy in the substrate, patch

	and adhesive respectively
U	Total strain energy of the system
$A_1, \cdots A_7$, $B_1, \cdots, B_{11}$,	Constants but are functions of r in case of
$C_1, \cdots C_4$, $D_1, \cdots, D_{11}$,	adhesive system with variable modulus
$F_1, \cdots, F_8$, $H_1, \cdots, H_{14}$	
η	Normalized distance from left end of the joint
$\sigma_{jk}^{(i)}$	Stress tensor in member 'i'((j,k) range over (r, θ, z))
$\epsilon_{jk}^{(i)}$	Strain tensor in member 'i'((j,k) range over (r, θ, z))
$S_{jk}^{(i)}$	Compliance tensor of the member $'i'$
subscript/superscript	
i	Variable number 1 for substrate, 2 for patch
	and 3 for the adhesive bond layer

Introduction

Presence of notches and cracks has a detrimental effect on the strength of the composite structures. Procedures have been established by airworthiness authorities that require regular inspections to ensure structural and component level integrity of aeronautical structures [1]. Small hairline defects can occur during manufacturing or due to thermo-mechanical loading during service life of the structure/component. These defects can influence the strength, stiffness and longevity of the structure. Replacing damaged aircraft parts is not always a feasible solution due to high cost and complications involved in the integration of new components. Commonly, adhesive patches are used to repair damaged parts or reinforce aeronautical structures [2; 3]. These patches are quite effective in delaying the growth of defects. Bonded repairs based on adhesively bonded composite patches or reinforcements can provide a highly structurally-efficient (strength and stiffness) and

cost-effective means of restoring residual strength to metallic or composite components. It has been reported that adhesively bonded patch can enhance the strength and stiffness of the damaged component upto 80% of the original strength [4; 5; 6; 7]. Estimation of the renewed strength of components repaired by adhesively bonded patches is very critical to aerospace industry [7; 8; 9]. Multiscale modeling strategies are essential to design and predict the performance of such composite materials/structures [see for e. g., [10; 11; 12]].

Experiments performed on the bonded repairs of stiffened thin 2024-T3 aluminium panel showed a 5-10 fold increase in fatigue life [13]. Reinforcing patch increases the strength and fatigue life of the component/ structure whilst reducing the stress intensity factor (SIF) near the crack tip. Several researchers used the stress fields or the SIF near the crack tip to estimate the fatigue life of crack-patch repair [14; 15; 16; 17; 5; 18]. Many analytical studies have been performed to determine the fatigue life and SIF for crack-patch repair assembly. Jones et al. [14; 15; 16; 17] studied the fatigue behaviour of a crack-patch system with patch as crack growth retarder and proposed a formula for SIF for multi-axial loading case. Jones and Chiu [14] examined the role of a full 3D analysis for efficient crack-patch design. Albedah et al. [19] developed an analytical formulation for the calculation of SIF at the crack tip of a bonded composite patch and compared their results with those of finite element predictions. Kwon and Hall [20] studied the influence of single-sided crack-patch in shifting the neutral axis of the system and subsequently stiffening of the component using mode-I strain energy release rate as a governing parameter. Fatigue life of a double-strap repair assembly under high-cycle fatigue is found to approximately double of the single-strap repairs [21].

Many researchers performed numerical simulations based on FE method to quantify the parameters governing the life of bonded crack-patch system (see for e.g.,[22]). Madani et al. [23] developed a numerical method to study the effect of adhesive and patch thicknesses on SIF and crack opening displacements. They found that by decreasing the thickness of adhesive the SIF can be decreased. A few researchers focused on the design of adhesive interlayer of the crack-patch

assembly in increasing the strength of the structure or component. FE analysis was carried out to predict the SIF as a function of adhesive properties and was found that the choice of adhesive and patch improves the performance of the structure [24]. Chukwujekwu and Bhogapurapu [25] performed finite element analysis of composite-patch repair to simulate crack propagation on the periphery of thick 2024 T3 clad aluminum aircraft panel and reported that the strain failure initiates in the adhesive layer first. Gu et al. [18] performed FE simulations on bonded composite repairs of single edge V-notch Al7075-T6 plate. They reported that the shear modulus and thickness of the adhesive play an important role in the efficient design of a composite crack-patch repair assembly. Ouinas et al. [26] conducted FE analysis on repair of crack emanating from the semi-circular lateral notch and identified that the properties of the adhesive are very crucial in the design of crack retarding patch. Several studies focused on modifying the geometry of the patch in order to optimize the structural performance of the patch-repair system (see for e. g., [27; 28; 29; 30]). Understanding the stress-state in the adhesive of a reinforcing patch covering a hairline defect is essential for the prediction of the repaired composite structures' remaining mechanical life and the fracture behaviour of a repaired component. Kumar et al. [31; 32; 33; 34] developed elasticity solutions to predict stress distribution within the adhesive interlayer of cylindrical systems using principle of minimum complementary energy (PMCE), while exactly satisfying all the traction and traction-free boundary conditions. The present study adopts a similar approach wherein the stress fields are made to satisfy both essential and natural boundary conditions. The complementary strain energy in the system is minimized using a variational approach assuming that the substrate, adhesive and patch are perfectly bonded to each other.

Initially, governing differential equation was formulated for a system composed of a homogeneous adhesive layer. For a system with a homogeneous adhesive layer, it was observed that the peak stresses in the adhesive occurs near the ends of the overlap (see e.g. [32]). These peak stress gradients along with stress peaks can be reduced using a graded adhesive interlayer [31]. Therefore, the later part of this study adopts the same idea of gradation of adhesive to model the

composite crack-patch repair assembly with an graded bondline so as to optimize the structural performance. However, note that the focus of this study is not on singular stress fields but on optimal material tailoring of the bondline adhesive.

1 Problem statement

In practice, aerospace components are subjected to a variety of loading conditions simultaneously. Assume, for simplicity, that the damaged composite or metallic component contains a through-thickness hairline defect. This defect in the component is repaired using an adhesively bonded single-side composite or metallic patch, as shown in Fig. 1. The interfaces between the adhesive and adherends are assumed to be perfect. These two interfaces are considered to be elastically weak where the stresses are continuous but displacement may or may not be continuous. The 3D axisymmetric crack-patch system is shown in Fig. 1. In Fig. 1, the substrate is represented as region (1), patch as region (2) and adhesive (bond layer) as region (3).

The axisymmtric assembly of substrate-adhesive-patch system is subjected to a radial far-field stress, σ_0 (see Fig. 2a). In order to set up the problem, a cylindrical coordinate system (r, θ, z) is introduced such that the origin of the coordinate system coincides with the center of the repair-patch as shown in Fig.2. It is assumed that the radial stress in each of the members to be a function of radial coordinate only, i.e. $\sigma_{rr}^{(1)}(r,z) = \sigma_{rr}^{(1)}(r)$ and $\sigma_{rr}^{(2)}(r,z) = \sigma_{rr}^{(2)}(r)$. In physical terms, this assumption ignores the bending deformations due to eccentric load path as the substrate is assumed to be restrained against the out of plane deformation. The classical example where this assumption could be valid is the use of stiffners to the substrate. Moreover, in this case, the presence of patch provides additional stiffness to the substrate reducing out of plane deformation. Since the thickness of adhesive is small relative to the substrate and the patch, the radial stress in the adhesive layer is neglected i.e $\sigma_{rr}^{(3)} = 0$.

In order to develop a tractable analytical model, it is further assumed that in each of the mem-

bers, radial stress is equal to the circumferential stress i.e., $\sigma_{rr}^{(i)}(r) = \sigma_{\theta\theta}^{(i)}(r)$ [see, for e.g.,[35]]. Under the influence of applied load, the substrate, patch and adhesive experience radial, peel and shear stresses denoted by $\sigma_{rr}^{(i)}(r), \sigma_{zz}^{(i)}(r,z)$ and $\tau_{rz}^{(i)}(r,z)$ respectively. Two crack-patch assemblies are studied, the first crack-patch assembly consists of a homogeneous adhesive and the second crack-patch assembly comprises a material tailored adhesive. The homogeneous bondline is referred to as monomodulus bondline (MMB) while the graded bondline is referred to as functionally modulus graded bondline (FMGB). The boundary conditions for the system shown in Fig. 2b are given in the subsequent section.

1.1 Boundary conditions

The peel and shear stresses are enforced to be continuous across the boundaries of different materials. The traction and traction-free conditions along with stress continuity conditions at interfaces of the crack-adhesive-patch assembly are given below.

Substrate (1):

$$\sigma_{rr}^{(1)} = \begin{cases} 0 & \text{if } r = \delta r \\ \sigma_0 & \text{if } r = a \end{cases} \qquad \tau_{rz}^{(1)} = \begin{cases} 0 & \text{if } r = \delta r \\ 0 & \text{if } r = a \end{cases} \Bigg| z \in (0, b) \tag{1}$$

$$\sigma_{zz}^{(1)} = \begin{cases} 0 & \text{if } z = 0 \\ \sigma_{zz}^{(3)} & \text{if } z = b \end{cases} \qquad \tau_{rz}^{(1)} = \begin{cases} 0 & \text{if } z = 0 \\ \tau_{rz}^{(3)} & \text{if } z = b \end{cases} \Bigg| r \in (0, a) \tag{2}$$

Adhesive (3):

$$\sigma_{rr}^{(3)} = \begin{cases} 0 & \text{if } r = a \end{cases} \qquad \tau_{rz}^{(3)} = \begin{cases} 0 & \text{if } r = a \end{cases} \Bigg| z \in (b, c) \tag{3}$$

$$\sigma_{zz}^{(3)} = \begin{cases} \sigma_{zz}^{(1)} & \text{if } z = b \\ \sigma_{zz}^{(2)} & \text{if } z = c \end{cases} \qquad \tau_{rz}^{(3)} = \begin{cases} \tau_{rz}^{(1)} & \text{if } z = b \\ \tau_{rz}^{(2)} & \text{if } z = c \end{cases} \Bigg| r \in (0, a) \tag{4}$$

Patch (2):

$$\sigma_{rr}^{(2)} = \left\{ \begin{array}{ll} 0 & \text{if } r = a \end{array} \right. \qquad \tau_{rz}^{(2)} = \left\{ \begin{array}{ll} 0 & \text{if } r = a \end{array} \right. \Bigg| z \in (c, d) \tag{5}$$

$$\sigma_{zz}^{(2)} = \left\{ \begin{array}{ll} \sigma_{zz}^{(3)} & \text{if } z = c \\ 0 & \text{if } z = d \end{array} \right. \qquad \tau_{rz}^{(2)} = \left\{ \begin{array}{ll} \tau_{rz}^{(3)} & \text{if } z = c \\ 0 & \text{if } z = d \end{array} \right. \Bigg| r \in (0, a) \tag{6}$$

Additionally, axisymmetry condition implies that the shear stress at $r = 0$ vanishes i.e.,

$$\tau_{rz}^{(2)}(0, z) = \tau_{rz}^{(3)}(0, z) = 0; \tag{7}$$

2 Stress fields

Under the static loading condition, the governing equilibrium equations (in the absence of body forces) for the axisymmetric assembly (see Fig. 2) can be simplified to the following, incorporating aforementioned assumptions.

$$\frac{\partial \sigma_{rr}^{(i)}}{\partial r} + \frac{\partial \tau_{rz}^{(i)}}{\partial z} = 0 \tag{8}$$

$$\frac{\partial \tau_{rz}^{(i)}}{\partial r} + \frac{\tau_{rz}^{(i)}}{r} + \frac{\partial \sigma_{zz}^{(i)}}{\partial z} = 0 \tag{9}$$

Solving the above two equilibrium equations [Eqns. (8) and (9)], we obtain general expressions for shear and peel stresses in each component of the assembly in terms of unknown radial stresses $\sigma_{rr}^{(i)}$.

$$\tau_{rz}^{(i)} = -z\sigma_{rr}^{(i)'} + K_1^{(i)} \tag{10}$$

$$\sigma_{zz}^{(i)} = \frac{z^2}{2}\left(\sigma_{rr}^{(i)''} + \frac{\sigma_{rr}^{(i)'}}{r}\right) - z\left(K_1^{(i)'} + \frac{K_1^{(i)}}{r}\right) + K_2^{(i)} \tag{11}$$

where, $()'$ and $()''$ represent first and second derivative of the function with respect to r, respectively. $K_1^{(i)}$ and $K_2^{(i)}$ are integration constants and they can be determined by satisfying the

traction-free and stress boundary conditions. The global radial force equilibrium implies that the sum of radial forces at any cross-section at radial distance r from axis of symmetry, in all members, is equal to the externally applied force.

$$\sigma_{rr}^{(1)} h_1 + \sigma_{rr}^{(2)} h_2 + \cancelto{0}{\sigma_{rr}^{(3)}} h_3 = \sigma_0 h_1 \tag{12}$$

Therefore, the relationship between radial stress in the substrate and patch is given by

$$\sigma_{rr}^{(2)} = \left(\frac{h_1}{h_2}\right)\sigma_0 - \sigma_{rr}^{(1)} \tag{13}$$

The constant $K_1^{(1)}$ is obtained using the shear stress-free condition at the bottom of the substrate i.e $\sigma_{rz}^{(1)}(r, 0) = 0 \left(K_1^{(1)} = 0\right)$. The resulting expression for the shear stress in the substrate is

$$\tau_{rz}^{(1)} = -z\sigma_{rr}^{(1)'} \tag{14}$$

Using the peel stress-free boundary condition at $z = 0$ i.e., $\sigma_{zz}^{(1)}(r, 0) = 0$ in Eqn.(11), we get $K_2^{(1)} = 0$. The resulting expression for the peel stress in substrate is given as

$$\sigma_{zz}^{(1)} = \frac{z^2}{2}\left(\sigma_{rr}^{(1)''} + \frac{\sigma_{rr}^{(1)'}}{r}\right) \tag{15}$$

The thickness of the adhesive interlayer is small and therefore the radial stress in the adhesive is considered to be negligible i.e $\sigma_{rr}^{(3)} = 0$. Using continuity of shear stress condition along the interface $z = b$, i.e $\tau_{rz}^{(1)}(r, b) = \tau_{rz}^{(3)}(r, b)$ in Eqn.(10), $K_1^{(3)}$ is obtained

$$K_1^{(3)} = -h_1\sigma_{rr}^{(1)'} \tag{16}$$

Consequently, the shear stress in the adhesive layer is expressed as

$$\tau_{rz}^{(3)} = -h_1\sigma_{rr}^{(1)'} \tag{17}$$

Applying continuity of peel stress condition at $z = b$ i.e $\sigma_{zz}^{(1)}(r, b) = \sigma_{zz}^{(3)}(r, b)$, in Eqn.(11), we

find $K_2^{(3)}$

$$K_2^{(3)} = -\frac{h_1^2}{2}\left(\sigma_{rr}^{(1)''} + \frac{\sigma_{rr}^{(1)'}}{r}\right) \tag{18}$$

Substitution of $K_2^{(3)}$ in Eqn.(11) yields expression for the peel stress in the adhesive interlayer as

$$\sigma_{zz}^{(3)} = -h_1\left(z - \frac{h_1}{2}\right)\left(\sigma_{rr}^{(1)''} + \frac{\sigma_{rr}^{(1)'}}{r}\right) \tag{19}$$

Again using shear stress continuity condition between the adhesive and the patch at $z = c$ i.e $\tau_{rz}^{(2)}(r, c) = \tau_{rz}^{(3)}(r, c)$ in Eqn.(10), we find the function $K_1^{(2)}(r)$

$$K_1^{(2)} = -\frac{ch_1}{h_2}\sigma_{rr}^{(1)'} - h_1\sigma_{rr}^{(1)'} \tag{20}$$

Substituting $K_1^{(2)}$ in Eqn.(10) for patch, we get shear stress in the patch as

$$\tau_{rz}^{(2)} = (c - z)\sigma_{rr}^{(2)'} - h_1\sigma_{rr}^{(1)'} \tag{21}$$

Substituting $\sigma_{rr}^{(2)'}$ obtained from Eqn.(13) into Eqn.(21), we get the shear stress in the patch in terms of only one unknown function $\sigma_{rr}^{(1)}$ as

$$\tau_{rz}^{(2)} = (c - z)\left(-\frac{h_1}{h_2}\sigma_{rr}^{(1)'}\right) - h_1\sigma_{rr}^{(1)'} \tag{22}$$

Applying the continuity of peel stress condition at the interface $r = c$ i.e $\sigma_{rr}^{(2)} = \sigma_{rr}^{(3)}$, in Eqn.(11) we find $K_2^{(2)}$ as

$$K_2^{(2)} = \frac{h_1}{2}\left(h_1 - \frac{c^2}{h_2}\right)\left(\sigma_{rr}^{(1)''} + \frac{\sigma_{rr}^{(1)'}}{r}\right) \tag{23}$$

Substituting $K_2^{(2)}$ in Eqn.(11) and subsequently reducing unknowns using global radial force equilibrium condition given by Eqn.(13), we get the expression for peel stress in the patch as

$$\sigma_{zz}^{(2)} = \left[-\left(\frac{z^2}{2}\frac{h_1}{h_2} - z\left(\frac{ch_1}{h} - h_1\right)\right) + \frac{h_1}{2}\left(h_1 - \frac{c^2}{h_2}\right)\right]\left(\sigma_{rr}^{(1)''} + \frac{\sigma_{rr}^{(1)'}}{r}\right) \tag{24}$$

Now all stress components in the entire assembly are defined in terms of a single unknown stress function $\sigma_{rr}^{(1)}$.

3 Variational method

A variational method is adopted in which a family of statically admissible stress fields are considered and complementary energy functional (U) is defined so that the elasto-static stress field minimizes the complementary energy functional (U). The complementary energy functional is constructed in terms of the primary unknown function $\sigma_{rr}^{(1)}$ (the radial stress in the substrate). Minimization of total complementary energy with respect to primary unknown $\sigma_{rr}^{(1)}$ yields the governing differential equation. The strain energy density of each of the members $'i'$ for an axisymmetric linear thermo-elastic solid is given by

$$U_d^{(i)} = \frac{1}{2}\Big[\sigma_{rr}^{(i)}\epsilon_{rr}^{(i)} + \sigma_{\theta\theta}^{(i)}\epsilon_{\theta\theta}^{(i)} + \sigma_{zz}^{(i)}\epsilon_{zz}^{(i)} + 2\epsilon_{rz}^{(i)}\sigma_{rz}^{(i)} + \alpha_r^{(i)}\Delta T\sigma_{rr}^{(i)} + \alpha_\theta^{(i)}\Delta T\sigma_{\theta\theta}^{(i)} + \alpha_z^{(i)}\Delta T\sigma_{zz}^{(i)}\Big] \quad (25)$$

The constitutive relationship for 3D transversely-isotropic linear-elastic material subjected to thermo-mechanical load is given by

$$\epsilon_{rr}^{(i)} = S_{11}^{(i)}\sigma_{rr}^{(i)} + S_{12}^{(i)}\sigma_{\theta\theta}^{(i)} + S_{13}^{(i)}\sigma_{zz}^{(i)} + \alpha_r^{(i)}\Delta T \quad (26a)$$

$$\epsilon_{\theta\theta}^{(i)} = S_{21}^{(i)}\sigma_{rr}^{(i)} + S_{22}^{(i)}\sigma_{\theta\theta}^{(i)} + S_{23}^{(i)}\sigma_{zz}^{(i)} + \alpha_\theta^{(i)}\Delta T \quad (26b)$$

$$\epsilon_{zz}^{(i)} = S_{31}^{(i)}\sigma_{rr}^{(i)} + S_{32}^{(i)}\sigma_{\theta\theta}^{(i)} + S_{33}^{(i)}\sigma_{zz}^{(i)} + \alpha_z^{(i)}\Delta T \quad (26c)$$

$$\epsilon_{rz}^{(i)} = S_{44}^{(i)}\tau_{rz}^{(i)} \quad (26d)$$

The components of compliance tensor $S_{jk}^{(i)}$ are given in Appendix-A. The elastic strains in each of the constituent members are evaluated in terms of stresses using linear-elastic transversely-isotropic constitutive behavior given by Eqn.(26). These elastic strain fields along with the corresponding stress fields for different components are used to calculate the elastic strain energy of each constituent of the assembly in terms of the unknown radial stress and its first/second order derivatives, i.e. $\sigma_{rr}^{(1)}, \sigma_{rr}^{(1)'}, \sigma_{rr}^{(1)''}$. The strain energy density of each constituent member is expressed

as a function of $\sigma_{rr}^{(1)}$ by substituting Eqn.(26) in Eqn.(25) as

$$U_d^{(i)} = \frac{(\sigma_{zz}^{(i)})^2}{E_z^{(i)}} + \frac{2(1-\nu_{r\theta}^{(i)})(\sigma_{rr}^{(i)})^2}{E_r^{(i)}} - \frac{4\nu_{rz}^{(i)}\sigma_{rr}^{(i)}\sigma_{zz}^{(i)}}{E_r^{(i)}} + \frac{(\tau_{rz}^{(i)})^2}{G_{rz}^{(i)}} \quad (27)$$

Therefore, the complementary energy in the substrate is written as

$$U^{(1)} = \pi \int_0^a \int_0^b \left[\frac{(\sigma_{zz}^{(1)})^2}{E_z^{(1)}} + \frac{2(1-\nu_{r\theta}^{(1)})(\sigma_{rr}^{(1)})^2}{E_r^{(1)}} - \frac{4\nu_{rz}^{(1)}\sigma_{rr}^{(1)}\sigma_{zz}^{(1)}}{E_r^{(1)}} + \frac{(\tau_{rz}^{(1)})^2}{G_{rz}^{(1)}} \right] r dr dz \quad (28)$$

By substituting the stress fields from the previous section, the strain energy in the substrate can be re-expressed in terms of the unknown radial stress as

$$U^{(1)} = \pi \int_0^a \left\{ A_1 \left(\frac{d^2}{dr^2}\sigma_{rr}^{(1)} \right)^2 r + \frac{A_2}{r} \left(\frac{d}{dr}\sigma_{rr}^{(1)} \right)^2 + A_3 \left(\frac{d}{dr}\sigma_{rr}^{(1)} \right) \left(\frac{d^2}{dr^2}\sigma_{rr}^{(1)} \right) + A_4 (\sigma_{rr}^{(1)})^2 + A_5 \left(\frac{d^2}{dr^2}\sigma_{rr}^{(1)} \right) \sigma_{rr}^{(1)} r + A_6 \left(\frac{d}{dr}\sigma_{rr}^{(1)} \right) \sigma_{rr}^{(1)} + A_7 \left(\frac{d}{dr}\sigma_{rr}^{(1)} \right)^2 r \right\} dr \quad (29)$$

where $A_1, A_2, \cdots A_7$ are constants and are defined in Appendix-A. Similarly, the complementary energy of the patch is given by

$$U^{(2)} = \pi \int_0^a \int_c^d \left[\frac{(\sigma_{zz}^{(2)})^2}{E_z^{(2)}} + \frac{2(1-\nu_{r\theta}^{(2)})(\sigma_{rr}^{(2)})^2}{E_r^{(2)}} - \frac{4\nu_{rz}^{(2)}\sigma_{rr}^{(2)}\sigma_{zz}^{(2)}}{E_r^{(2)}} + \frac{(\tau_{rz}^{(2)})^2}{G_{rz}^{(2)}} \right] r dr dz \quad (30)$$

Again substituting appropriate stress fields from the previous section into the above equation, the strain energy in the patch can be written as

$$U^{(2)} = \pi \int_0^a \left\{ B_1 \left(\frac{d^2}{dr^2}\sigma_{rr}^{(1)} \right)^2 r + \frac{B_2}{r} \left(\frac{d}{dr}\sigma_{rr}^{(1)} \right)^2 + B_3 \left(\frac{d}{dr}\sigma_{rr}^{(1)} \right) \left(\frac{d^2}{dr^2}\sigma_{rr}^{(1)} \right) + B_4 (\sigma_{rr}^{(1)})^2 r + B_5 r + B_6 \sigma_{rr}^{(1)} r + B_7 \left(\frac{d^2}{dr^2}\sigma_{rr}^{(1)} \right) r + B_8 \left(\frac{d}{dr}\sigma_{rr}^{(1)} \right) + B_9 \sigma_{rr}^{(1)} \left(\frac{d^2}{dr^2}\sigma_{rr}^{(1)} \right) r + B_{10} \sigma_{rr}^{(1)} \left(\frac{d}{dr}\sigma_{rr}^{(1)} \right) + B_{11} \left(\frac{d}{dr}\sigma_{rr}^{(1)} \right)^2 r \right\} dr \quad (31)$$

where $B_1, B_2, \cdots B_{11}$ are constants and are defined in Appendix-A. The complementary energy of

the adhesive also is given by

$$U^{(3)} = \pi \int_0^a \int_b^c \left[\frac{(\sigma_{zz}^{(3)})^2}{E^{(3)}} + \frac{2(1-\nu^{(3)})(\cancelto{0}{\sigma_{rr}^{(3)}})^2}{E^{(3)}} - \frac{4\nu_{rz}^{(3)}\cancelto{0}{\sigma_{rr}^{(3)}}\sigma_{zz}^{(3)}}{E^{(3)}} + \frac{(\tau_{rz}^{(3)})^2}{G^{(3)}} \right] r dr dz \qquad (32)$$

The stress fields for the adhesive from the previous section are plugged into the above equation, to obtain the strain energy in the adhesive layer

$$U^{(3)} = \pi \int_0^a \left\{ C_1 \left(\frac{d^2}{dr^2}\sigma_{rr}^{(1)} \right)^2 r + \frac{C_2}{r}\left(\frac{d}{dr}\sigma_{rr}^{(1)} \right)^2 + C_3 \left(\frac{d}{dr}\sigma_{rr}^{(1)} \right)\left(\frac{d^2}{dr^2}\sigma_{rr}^{(1)} \right) + C_4 \left(\frac{d}{dr}\sigma_{rr}^{(1)} \right)^2 r \right\} dr \qquad (33)$$

where C_1, C_2, C_3, and C_4 are constants and are given in Appendix-A. The total complementary strain energy of the system U is obtained by adding the energy contribution from individual component and is given by

$$\begin{aligned} U = \pi \int_0^a \Bigg\{ & D_1 \left(\frac{d^2}{dr^2}\sigma_{rr}^{(1)} \right)^2 r + \frac{D_2}{r}\left(\frac{d}{dr}\sigma_{rr}^{(1)} \right)^2 + D_3 \left(\frac{d}{dr}\sigma_{rr}^{(1)} \right)\left(\frac{d^2}{dr^2}\sigma_{rr}^{(1)} \right) \\ & + D_4(\sigma_{rr}^{(1)})^2 r + D_5 r + D_6 \sigma_{rr}^{(1)} r + D_7 \left(\frac{d^2}{dr^2}\sigma_{rr}^{(1)} \right) r + D_8 \left(\frac{d}{dr}\sigma_{rr}^{(1)} \right) \\ & + D_9 \sigma_{rr}^{(1)} \left(\frac{d^2}{dr^2}\sigma_{rr}^{(1)} \right) r + D_{10}\sigma_{rr}^{(1)} \left(\frac{d}{dr}\sigma_{rr}^{(1)} \right) + D_{11} \left(\frac{d}{dr}\sigma_{rr}^{(1)} \right)^2 r \Bigg\} dr \end{aligned} \qquad (34)$$

where the constants $D_1, D_2, \cdots D_{11}$ are defined in Appendix-A. The total complementary energy U is minimized with respect to the unknown radial stress in the substrate $\sigma_{rr}^{(1)}$ using the Euler-Lagrange variational principle to obtain the the following governing ODE

$$\begin{aligned} \frac{1}{r^2} \Bigg\{ & F_1 \left(\frac{d^2}{dr^2}\sigma_{rr}^{(1)}(r) \right) r^3 + F_2 \left(\frac{d}{dr}\sigma_{rr}^{(1)}(r) \right) r^2 + F_3 r^3 \sigma_{rr}^{(1)}(r) + F_4 r^3 + F_5 \frac{d}{dr}\sigma_{rr}^{(1)}(r) \\ & + F_6 \left(\frac{d^2}{dr^2}\sigma_{rr}^{(1)}(r) \right) r + F_7 \left(\frac{d^3}{dr^3}\sigma_{rr}^{(1)}(r) \right) r^2 + F_8 \left(\frac{d^4}{dr^4}\sigma_{rr}^{(1)}(r) \right) r^3 \Bigg\} = 0 \end{aligned} \qquad (35)$$

where $F_1, F_2, \cdots F_8$ are constants and they depend upon the material and geometrical properties

as well as the loading conditions. The above governing equation is a linear fourth order ordinary differential equation (ODE) with known constant coefficients. This ODE represents the case of crack-patch repair assembly with homogeneous adhesive interlayer. The governing ODE was solved using Maple Version 16. Since the above ODE has $1/r^2$ singularity, middefer solver in Maple to solve the ODE was used. Middefer is essentially a midpoint method to solve harmless singularities. The strength of singularity at the crack tip is further reduced assuming a finite radius of the crack (= 0.1 *mm*) instead of a 1D crack.

The boundary conditions for the governing ODE (Eqn.(35)) is determined from the boundary condition for the radial stress in the substrate and they are given by

$$\sigma_{rr}^{(1)}(\delta r) = 0; \qquad \sigma_{rr}^{(1)}(a) = \sigma_0 \tag{36}$$

For remaining boundary conditions, we use shear stress at $r = \delta r$ and $r = a$ in Eqn. (14) to obtain

$$\tau_{rz}^{(1)}(\delta r) = -\delta r\, \sigma_{rr}^{(1)'}(\delta r) = 0; \;\; \tau_{rz}^{(1)}(a) = -\delta r\, \sigma_{rr}^{(1)'}(a) = 0 \tag{37}$$

From the above equation, it is clear that the radial stress derivatives $\sigma_{rr}^{(1)'}$ vanishes at the boundaries $r = 0$ and $r = a$. Therefore, the governing ODE is solved using the boundary conditions given by Eqns.(36) and (37) to obtain unknown radial stress $\sigma_{rr}^{(1)}$ and hence the shear and peel stresses in each constituent of the substrate-adhesive-patch assembly using Eqns (10) and (11), respectively.

4 Material Tailored Adhesive Layer

A few researchers studied bi-adhesive joints considering a single step variation of adhesive's modulus over the bond length to reduce the stress peaks and their gradients near the ends of the overlap using a compliant adhesive near the ends of the overlap (see for e.g.,[36; 37]). Effect of gradually varying the adhesive modulus along the bondline was also studied using theoretical and experimental studies [31; 38; 39; 40]. Following Kumar [31], the elastic modulus of FMGB adhesive is

graded in the radial direction such that it has a minimum value both at edge and center as shown in Fig. 3. Although, the Young's modulus of the adhesive is graded along the bond radius, the Poisson's ratio of the adhesive is assumed to be constant over the entire adhesive volume. However, it should still be noted that the adhesive is isotropic. The bondline adhesive can be graded with a variety of modulus profiles and investigated using the present model in order to identify an optimal scheme. A parabolic profile is chosen to test the effectiveness of the gradation scheme in order to demonstrate utility of interface tailored crack-patch repair systems. This parabolic profile for the adhesive modulus $E^{(3)}$ is given by the following equation

$$E^{(3)}(r) = 4(E_c - E_0)\left(\frac{r}{a}\right)\left[1 - \left(\frac{r}{a}\right)\right] + E_0; \tag{38}$$

where, E_0 and E_c are the minimum and maximum values of the modulus of the adhesive chosen respectively. The strain energy of the graded adhesive is obviously different from the graded one. The above formulation for the homogeneous adhesive can still be used by using a smooth function $E^{(3)}(r)$ instead of a constant $E^{(3)}$. Consequently, explicit form of the governing ODE of the present model with FMGB is given by

$$\begin{aligned}\frac{1}{r^2}\Bigg[H_1\left(\frac{d^2}{dr^2}\sigma_{rr}^{(1)}(r)\right)r^3 + H_2\left(\frac{d}{dr}\sigma_{rr}^{(1)}(r)\right)r^2 + H_3 r^3\sigma_{rr}^{(1)}(r) + H_4 r^3 + H_5\frac{d}{dr}\sigma_{rr}^{(1)}(r) \\ + H_6\left(\frac{d^2}{dr^2}\sigma_{rr}^{(1)}(r)\right)r + H_7\left(\frac{d}{dr}\sigma_{rr}^{(1)}(r)\right)r + H_8\left(\frac{d^2}{dr^2}\sigma_{rr}^{(1)}(r)\right)r^2 + H_9\sigma_{rr}^{(1)}r^2 \\ + H_{10}\left(\frac{d}{dr}\sigma_{rr}^{(1)}(r)\right)r^3 + H_{11}\left(\frac{d^3}{dr^3}\sigma_{rr}^{(1)}(r)\right)r^3 + H_{12} + H_{13}\left(\frac{d^3}{dr^3}\sigma_{rr}^{(1)}(r)\right)r^2 + \\ H_{14}\left(\frac{d^4}{dr^4}\sigma_{rr}^{(1)}(r)\right)r^3\Bigg] = 0\end{aligned} \tag{39}$$

where the variable coefficients $H_1, H_2, \cdots H_{14}$ are defined in Appendix-A. These coefficients are functions of r and are dependent on the material and geometrical properties as well as loading conditions. The order of singularity of the governing ODE depends on the coefficients $H_1, H_2, \cdots H_{14}$ which in turn depend on the gradation scheme chosen. For example, the order of singularity of the

governing ODE in case of MMB adhesive is two.

5 Results and Discussion

5.1 Finite element analysis

Axisymmetric finite element analysis of the crack-patch assembly with a through-thickness defect in the substrate was carried out using Abaqus FEA. The crack-patch assembly was assumed to be linear elastic and isotropic for the both the graded and homogeneous cases. A 4-node bilinear axisymmetric quadrilateral element (CAX4R) was used for both adherends and adhesive to discretize the domain with approximately 115000 elements. The mesh was biased towards the overlap end considering the effect of singularity [41]. The gradation of adhesive along the bond length is achieved using a user written material model called "UMAT". The gradation profile used in FEA is essentially same as the one used in the analytical model given by Eqn.(38). The assembly was subjected to same load as that of the analytical model. A linear static elastic analysis of crack-patch assembly was carried out by using the properties given in Table. 1. The radial stresses in the substrate and the patch are presented in Fig. 5 which shows that there is an equal and opposite reaction at the patch section due to simplifying assumption that $\sigma_{rr} = \sigma_{\theta\theta}$. The results were compared with the developed theoretical model as shown in Figs. 6a and 6b respectively. A small discrepancy in the results obtained from the analytical model from that of the FEA is due to simplifying assumptions employed and omission of bending effects in the adherends.

5.2 Homogeneous bondline

Henceforth, we use the developed analytical model. Consider a substrate made of an aluminum alloy with a hairline through-thickness crack of radius $\delta r = 0.1$ mm repaired by an aluminum patch using a homogeneous epoxy adhesive. The geometric and material properties of the crack-

patch assembly are given in Table (1). Fig. 7 shows the distribution of shear and peel stresses at three different surfaces viz. 1. mid-surface of adhesive, 2. interface of the substrate and adhesive and 3. interface of the adhesive and patch along the bond radius for $\sigma_0 = 100$ MPa. In these figures, normalized shear and peel stresses are plotted against the normalized overlap distance. Note that the peak adhesive stresses are concentrated both at the center and the edge of the patch. Peak shear and peel stresses in the adhesive at the center arise due to the presence of crack in the substrate. From Fig. 7*a*, it can be seen that the middle portion of the bondline ($\eta = 0.3$ to 0.65) has almost zero shear stress and suggest that the properties of the adhesive can be tailored over the bond radius so as to effectively use the material in the middle portion of the bond radius. Shear stress distribution shown in Fig. 7a also demonstrates that the present analytical model satisfies the traction-free conditions at $r = 0$ and $r = a$. The shear stress is almost constant over the thickness of the bondline unlike the peel stress as can be seen in Eqn.(17).

5.2.1 Transversely isotropic adherends

To demonstrate an implementation of the present model for the repair of composite components with isotropic or anisotropic patches,different combinations of substrate-patch materials were considered whilst keeping the geometric properties same as the previous example (see Table. 3 for the properties considered [42]). The composite patch considered herein is relatively compliant compared to the aluminum therefore the adhesive stresses are higher while using a composite patch with an isotropic substrate (see Figs. 8a and 8b).

The interlaminar stress distribution presented in Figs. 7a and 7b show the existence of steep gradients near the edge of the patch due to mismatch in material properties. These peak stresses are function of properties of the adhesive and patch for a given substrate and loading conditions. To predict the influence of adhesive and patch properties on the stress fields, a parametric study was conducted by varying the following parameters.

- Thickness of the patch (h_2).
- Thickness of the adhesive (h_3).
- Elastic modulus of the adhesive ($E^{(3)}$)

Thickness of the patch (h_2)

The material and geometric properties used for this study are given in Table 1. Analyses were performed varying the patch thickness h_2 from 1 mm to 3 mm i.e., h_2 = {1.0 1.5 2.0 2.5 3.0}mm, keeping all other parameters the same. The shear and peel stress distribution along the bond radius as a function of patch thickness is shown in Fig. 9. As h_2 increases, the peak shear and peel stresses as well as their gradients decrease. The increase in h_2 reduces the peak stresses near the crack tip whereas it has little influence on the stress distribution near the end of the patch. The peak shear stress decreases by 66% while peak peel stress decreases by 76% when h_2 is increased from 1 mm to 3 mm for the parameters considered herein. This parametric study helps us to identify an ideal h_2 for a given system and loading conditions.

Thickness of the adhesive (h_3)

Analyses were performed under the same loading condition using the properties given in Table 1 by varying the thickness of the adhesive from 0.05 mm to 0.5 mm i.e., h_3 = {0.05 0.1 0.2 0.25 0.5}mm. The shear and peel stress distribution at the mid-surface of the adhesive along the bond radius as a function of adhesive thickness is shown in Figs. 10a and 10b respectively. The peak shear stress decreases by 18% and 35% at the center and near the edge of the bondline respectively when the thickness of the adhesive increased from 0.05 mm to 0.5 mm. However, reduction in peak peel stress is not significant.

Elastic modulus of the adhesive ($E^{(3)}$)

The Young's modulus of the adhesive is varied from 600 MPa to 3920 MPa and analyses were performed keeping all other geometric and material properties the same while the substrate is subjected to a far field stress σ_0 = 100 MPa. The shear and peel stress distribution at the mid-surface of the adhesive layer over the bond radius is shown in Figs. 11a and 11b respectively as a function of Young's modulus of adhesive. As the adhesive modulus $E^{(3)}$ increases, the shear stress near the crack-tip does not change significantly whereas it increases by 150 % near the edge of the patch. The peak peel stress does not change significantly with the increase in modulus of the adhesive.

The shear stress peaks observed at the center and near the edge of the overlap suggest that the stress concentration can be minimized and the distributions can become more uniform over the bond radius by appropriately tailoring the material properties of the bondline over the radius. Identified stress concentration zones are shown in Fig. 3.

5.3 Graded bondline

In case of homogeneous bondline, adhesive stresses are concentrated both at the center (where crack exists) and near the free edge of the overlap. The concentration of the shear/peel stresses at the edge may lead to delamination of the patch. The peak adhesives stresess at the center around the crack may lead to damage/crack propagation. One of the ways to avoid such stress concentrations is selective material tailoring. By making the stress concentration zones with compliant adhesive, we could diffuse the stresses. However, in this case, in order to retain the load carrying capacity, the portion of the adhesive away from the stress concentration zones needs to be stiffened. Therefore, the modulus of adhesive layer is graded radially such that it has a minimum value of modulus in the stress concentration zones. The enhanced stiffness of the adhesive layer at a location $a/2$ from the center shown in Fig. 3, favours the redistribution of shear stresses away from the edge and

crack.

The elastic modulus of the adhesive layer is radially graded such that it has a minimum value (E_0 = 280 MPa) both at the center and the edge while it has a maximum value (E_m = 2700 MPa) away from the stress concentration zones using Eqn.(38) (see Fig. 3). The Poisson's ratio of adhesive is assumed to be constant ν = 0.35 although the adhesive is graded. Analyses were performed keeping all other geometric and material properties the same as those of homogeneous bondline case under a far field stress σ_0 = 100 MPa. Figs. 12 through 14 show the comparison of shear and peel stresses obtained from FMGB model with those of MMB model over the bond radius at the mid-surface and the interfaces of adhesive. These figures indicate that the adhesive stresses can be significantly reduced by tailoring the elastic modulus along the bondline. For the modulus profile adopted here, the peak shear stress decreases by 26 % while the peak peel stress decreases by 37 % along with the reduction in steep stress gradients. A parametric study was performed as before with FMGB adhesive layer to study the influence of modulus gradation on adhesive stresses.

5.3.1 Thickness of the patch (h_2)

Analysis were performed for FMGB case using the same geometrical and material properties as those of MMB model for various patch thicknesses h_2 under the same load. The shear and peel stress distribution along the bond radius as a function of thickness of repair patch is shown in Figs. 15a and 15b respectively. Fig. 15 indicates that shear stress peak reduces by 55 % while the peak peel stress reduces by 61 % when the thickness of the patch is increased from 1 mm to 3 mm. Figs. 16a and 16b show the variation of peak shear and peel stresses respectively in the bondline as a function of patch thickness for both FMGB and MMB models. These figures indicate that the FMGB bondline can increase the load carrying capacity more than the MMB bondline. For both FMGB and MMB cases, the peak adhesive stresses decrease with increase in patch thickness, although the rate at which the peak adhesive stresses decrease in FMGB case is lower than those

of MMB model.

5.3.2 Thickness of the adhesive (h_3)

Thickness of the FMGB adhesive was varied and analyses was performed keeping all other parameters the same as before. The shear and peel stress distribution along the bond radius as a function of the adhesive thickness is shown in Figs. 17a and 17b respectively. The peak shear stress decreases with the increase in adhesive thickness similar to MMB system. However, it should be noted that the shear stress decreases by 45 % unlike the MMB case in which the peak shear stress decreases by 18 % when the adhesive thickness increased from 0.05 to 0.5 mm. The reduction in peak peel stress is also significant for FMGB case (46 %). Recall that the peak peel stress of MMB crack-patch assembly does not vary much with adhesive thickness for the chosen geometry and materials (See Fig. 10b). Figs. 18a and 18b show the variation of peak shear and peel stresses respectively in the adhesive as a function of adhesive thickness for both FMGB and MMB models. For the parameters used herein, the peak adhesive stresses decrease with increase of adhesive thickness upto 0.25 mm and thence they remain constant with further increase in thickness of the adhesive.

5.4 Stiffness mismatch between the patch and the substrate

The effect of stiffness mismatch on the adhesive stresses was studied considering three different crack-patch assemblies with $\frac{E_2 h_2}{E_1 h_1} = \{0.7\ 1.0\ 1.43\}$. The adhesive and geometric properties were same as those of the previous example and the material properties of the adherends are given in Table.2. The shear and peel stresses plotted along the mid-surface of adhesive (see, Fig. 19) for the above assemblies show clearly that the assembly with stiffness ratio greater than 1 has the least stress peaks. Therefore, the reinforcing patch should have a stiffness greater than the substrate.

6 Conclusions

The principle of minimum complementary energy in conjunction with a variational method is employed to theoretically determine the stresses in each of the constituents of 3D axisymmetric single-side composite patch-repair assembly. The concept of gradation of adhesive elastic modulus is successfully applied in reducing the stress concentration at the edge and center of the patch, by redistributing the stresses in the adhesive. Material tailoring of bondline significantly reduces peak adhesive stresses. In this study, a specific gradation scheme is demonstrated to minimize peak stresses in the adhesive but the formulation is generic and can be used to study a variety of gradation schemes. Thermal or thermo-mechanical stresses can also be studied using the present approach. The results of the parametric study indicate that as the patch thickness increases, the peak adhesive stresses decrease in both MMB and FMGB systems, but to a greater extent in FMGB bondlines, for chosen geometric and material properties of the assembly. Results indicate that both the strength and longevity of the repaired systems can be significantly improved by introducing graded bondlines. The proposed analytical solution neglects bending deformations and this limits the utility of the analytical solution to only systems experiencing negligible bending deformations. Availability of multi-material 3D printers and rapid development in 3D printing technology of composite materials enable the design of such material tailored structural systems as demonstrated elsewhere [43; 44].

7 Acknowledgement

The authors wish to acknowledge the support of the Masdar Institute of Science and Technology through MI/MIT cooperative agreement (Award No:12MAMA1).

Appendix-A

7.1 Compliance tensor

The compliance tensor for the member $'i'$ is given by

$$S_{jk}^{(i)} = \begin{bmatrix} \frac{1}{E_r^{(i)}} & -\frac{\nu_{r\theta}^{(i)}}{E_\theta^{(i)}} & -\frac{\nu_{rz}^{(i)}}{E_z^{(i)}} & 0 \\ -\frac{\nu_{\theta r}^{(i)}}{E_r^{(i)}} & \frac{1}{E_\theta^{(i)}} & -\frac{\nu_{\theta z}^{(i)}}{E_z^{(i)}} & 0 \\ -\frac{\nu_{zr}^{(i)}}{E_r^{(i)}} & -\frac{\nu_{z\theta}^{(i)}}{E_\theta^{(i)}} & \frac{1}{E_z^{(i)}} & 0 \\ 0 & 0 & 0 & \frac{1}{G_{rz}^{(i)}} \end{bmatrix} \tag{40}$$

7.2 Constants that depend upon geometrical and material properties as well as loading conditions

$$A_1 = A_2 = \pi \frac{1}{E_z^{(1)}} \int_0^b \frac{z^4}{4} dz \tag{41a}$$

$$A_3 = \pi \frac{1}{E_z^{(1)}} \int_0^b \frac{z^4}{2} dz \tag{41b}$$

$$A_4 = \pi \frac{2(1-\nu_{r\theta}^{(1)})}{E_r^{(1)}} \int_0^b dz \tag{41c}$$

$$A_5 = A_6 = -\pi \frac{4\nu_{rz}^{(1)})}{E_r^{(1)}} \int_0^b \frac{z^2}{2} dz \tag{41d}$$

$$A_7 = \pi \frac{1}{G_{rz}^{(1)}} \int_0^b z^2 dz \tag{41e}$$

$$B_1 = B_2 = \pi \frac{1}{E_z^{(2)}} \int_c^d \left[-\left(\frac{z^2}{2}\frac{h_1}{h_2} - z\left(\frac{ch_1}{h} - h_1\right)\right) + \frac{h_1}{2}\left(h_1 - \frac{c^2}{h_2}\right)\right]^2 dz \tag{42a}$$

$$B_3 = \pi \frac{1}{E_z^{(2)}} \int_c^d 2\left[-\left(\frac{z^2}{2}\frac{h_1}{h_2} - z\left(\frac{ch_1}{h} - h_1\right)\right) + \frac{h_1}{2}\left(h_1 - \frac{c^2}{h_2}\right)\right]^2 dz \tag{42b}$$

$$B_4 = \pi \frac{2(1-\nu_{r\theta}^{(2)})}{E_r^{(2)}} \int_c^d dz \tag{42c}$$

$$B_5 = \pi \frac{4(1-\nu_{r\theta}^{(2)})}{E_r^{(2)}} \left(\frac{\sigma_0 h_1}{h_2}\right)^2 \int_c^d dz \tag{42d}$$

$$B_6 = -\pi \frac{2(1-\nu_{r\theta}^{(2)})}{E_r^{(2)}} \left(\frac{2\sigma_0 h_1}{h_2}\right) \int_c^d dz \tag{42e}$$

$$B_7 = B_8 = -\pi \frac{4\nu_{rz}^{(2)}}{E_r^{(2)}} \frac{\sigma_0 h_1}{h_2} \int_c^d \left[-\left(\frac{z^2}{2}\frac{h_1}{h_2} - z\left(\frac{ch_1}{h} - h_1\right)\right) + \frac{h_1}{2}\left(h_1 - \frac{c^2}{h_2}\right)\right] dz \tag{42f}$$

$$B_9 = B_{10} = \pi \frac{4\nu_{rz}^{(2)}}{E_r^{(2)}} \int_c^d \left[-\left(\frac{z^2}{2}\frac{h_1}{h_2} - z\left(\frac{ch_1}{h} - h_1\right)\right) + \frac{h_1}{2}\left(h_1 - \frac{c^2}{h_2}\right)\right] dz \tag{42g}$$

$$B_{11} = \pi \frac{1}{G_{rz}^{(2)}} \int_c^d \left[\frac{(z-c)h_1}{h_2} - h_1\right]^2 dz \tag{42h}$$

$$C_1 = C_2 = \pi \frac{h_1^2}{E^{(3)}} \int_b^c \left(\frac{h_1}{2} - z\right)^2 dz \tag{43a}$$

$$C_3 = \pi \frac{2h_1^2}{E^{(3)}} \int_b^c \left(\frac{h_1}{2} - z\right)^2 dz \tag{43b}$$

$$C_4 = \frac{2\pi h_1^2 (1+\nu^{(3)})}{E^{(3)}} \int_b^c dz \tag{43c}$$

$$D_1 = A_1 + B_1 + C_1 \tag{44a}$$

$$D_2 = A_2 + B_2 + C_2 \tag{44b}$$

$$D_3 = A_3 + B_3 + C_3 \tag{44c}$$

$$D_4 = A_4 + B_4 \tag{44d}$$

$$D_5 = B_5 \tag{44e}$$

$$D_6 = B_6 \tag{44f}$$

$$D_7 = B_7 \tag{44g}$$

$$D_8 = B_8 \tag{44h}$$

$$D_9 = A_5 + B_9 \tag{44i}$$

$$D_{10} = A_6 + B_{10} \tag{44j}$$

$$D_{11} = A_7 + B_{11} + C_4 \tag{44k}$$

$$F_1 = F_2 = 2D_9 - 2D_{11} \tag{45a}$$

$$F_3 = 2D_4 \tag{45b}$$

$$F_4 = D_6 \tag{45c}$$

$$F_5 = 2D_2 \tag{45d}$$

$$F_6 = -2D_2 \tag{45e}$$

$$F_7 = 4D_1 \tag{45f}$$

$$F_8 = 2D_1 \tag{45g}$$

$$H_1 = 2D_1'' + 2D_9 - 2D_{11} \tag{46a}$$

$$H_2 = 2D_3'' + 2D_9 - 2D_{11} \tag{46b}$$

$$H = 2D_4 + D_9'' \tag{46c}$$

$$H_4 = D_6 + D_7'' \tag{46d}$$

$$H_5 = 2D_2 \tag{46e}$$

$$H_6 = -2D_2 \tag{46f}$$

$$H_7 = -2D_2' - 2D_2 \tag{46g}$$

$$H_8 = 3D_1' + D_3' \tag{46h}$$

$$H_9 = 2D_9' - D_{10}' \tag{46i}$$

$$H_{10} = 2D_9 - 2D_{11} - 2D_{11}' \tag{46j}$$

$$H_{11} = 4D_1' \tag{46k}$$

$$H_{12} = 2D_7' \tag{46l}$$

$$H_{13} = 4D_1' \tag{46m}$$

$$H_{14} = 2D_1 \tag{46n}$$

References

[1] KB Katnam, LFM Da Silva, and TM Young. Bonded repair of composite aircraft structures: A review of scientific challenges and opportunities. *Progress in Aerospace Sciences*, 61:26–42, 2013.

[2] Alan Baker. Bonded composite repair of fatigue-cracked primary aircraft structure. *Composite Structures*, 47(1):431–443, 1999.

[3] A Baker et al. *Bonded repair of aircraft structures*, volume 7. Springer Science & Business Media, 2012.

[4] MA Caminero, M Lopez-Pedrosa, C Pinna, and C Soutis. Damage monitoring and analysis of composite laminates with an open hole and adhesively bonded repairs using digital image correlation. *Composites Part B: Engineering*, 53:76–91, 2013.

[5] H Hosseini-Toudeshky and B Mohammadi. Mixed-mode numerical and experimental fatigue crack growth analyses of thick aluminium panels repaired with composite patches. *Composite Structures*, 91(1):1–8, 2009.

[6] M Benachour, N Benachour, M Benguediab, and FZ Seriari. Prediction of fatigue crack growth of repaired al-alloy structures with double sides. *Physics Procedia*, 55:83–89, 2014.

[7] Heung Soo Kim, Maenghyo Cho, Jaehun Lee, Antoine Deheeger, Michel Grédiac, and Jean-Denis Mathias. Three dimensional stress analysis of a composite patch using stress functions. *International Journal of Mechanical Sciences*, 52(12):1646–1659, 2010.

[8] MN Charalambides, AJ Kinloch, and FL Matthews. Adhesively-bonded repairs to fibre-composite materials ii. finite element modelling. *Composites Part A: Applied Science and Manufacturing*, 29(11):1383–1396, 1998.

[9] Alan Baker, Andrew J Gunnion, and John Wang. On the certification of bonded repairs to primary composite aircraft components. *The Journal of Adhesion*, 91(1-2):4–38, 2015.

[10] G Pal and S Kumar. Modeling of carbon nanotubes and carbon nanotube–polymer composites. *Progress in Aerospace Sciences*, 80:33–58, 2016.

[11] SI Kundalwal and S Kumar. Multiscale modeling of stress transfer in continuous microscale fiber reinforced composites with nano-engineered interphase. *Mechanics of Materials*, 102:117–131, 2016.

[12] Priyank Upadhyaya and S Kumar. Micromechanics of stress transfer through the interphase in fiber-reinforced composites. *Mechanics of Materials*, 89:190–201, 2015.

[13] V Sabelkin, S Mall, and JB Avram. Fatigue crack growth analysis of stiffened cracked panel repaired with bonded composite patch. *Engineering Fracture Mechanics*, 73(11):1553–1567, 2006.

[14] Rhys Jones and Wing Kong Chiu. Composite repairs to cracks in thick metallic components. *Composite Structures*, 44(1):17–29, 1999.

[15] Rhys Jones and D Peng. Composite repairs to cracked holes under bi-axial loading. *Composite structures*, 57(1):459–464, 2002.

[16] Rhys Jones, K Krishnapillai, and Susan Pitt. Crack patching: predicting fatigue crack growth. *Theoretical and applied fracture mechanics*, 45(2):79–91, 2006.

[17] Rhys Jones and Susan Pitt. Crack patching revisited. *Composite structures*, 76(3):218–223, 2006.

[18] Linxia Gu, Ananth Ram Mahanth Kasavajhala, and Shijia Zhao. Finite element analysis of cracks in aging aircraft structures with bonded composite-patch repairs. *Composites Part B: Engineering*, 42(3):505–510, 2011.

[19] A Albedah, F Benyahia, H Dinar, and B Bachir Bouiadjra. Analytical formulation of the stress intensity factor for crack emanating from central holes and repaired with bonded composite patch in aircraft structures. *Composites Part B: Engineering*, 45(1):852–857, 2013.

[20] YW Kwon and BL Hall. Analyses of cracks in thick stiffened plates repaired with single-sided composite patch. *Composite Structures*, 119:727–737, 2015.

[21] RDF Moreira, MFSF de Moura, RL Fernandes, MAV Figueiredo, and JPM Gonçalves. Numerical and experimental analyses of composite bonded double-strap repairs under high-cycle fatigue. *The Journal of Adhesion*, (just-accepted), 2016.

[22] Vishwajeet S Bhise, Mohammad Kashfuddoja, and M Ramji. Optimization of circular composite patch reinforcement on damaged carbon fiber reinforced polymer laminate involving both mechanics-based and genetic algorithm in conjunction with 3d finite element analysis. *Journal of Composite Materials*, page 0021998313501922, 2013.

[23] K Madani, S Touzain, X Feaugas, M Benguediab, and M Ratwani. Numerical analysis for the determination of the stress intensity factors and crack opening displacements in plates repaired with single and double composite patches. *Computational Materials Science*, 42(3):385–393, 2008.

[24] T Achour, B Bachir Bouiadjra, and B Serier. Numerical analysis of the performances of the bonded composite patch for reducing stress concentration and repairing cracks at notch. *Computational materials science*, 28(1):41–48, 2003.

[25] A Chukwujekwu Okafor and Hari Bhogapurapu. Design and analysis of adhesively bonded thick composite patch repair of corrosion grind-out and cracks on 2024 t3 clad aluminum aging aircraft structures. *Composite structures*, 76(1):138–150, 2006.

[26] D Ouinas, B Bachir Bouiadjra, B Serier, and M SaidBekkouche. Comparison of the effectiveness of boron/epoxy and graphite/epoxy patches for repaired cracks emanating from a semicircular notch edge. *Composite structures*, 80(4):514–522, 2007.

[27] A Chukwujekwu Okafor, Navdeep Singh, UE Enemuoh, and SV Rao. Design, analysis and performance of adhesively bonded composite patch repair of cracked aluminum aircraft panels. *Composite Structures*, 71(2):258–270, 2005.

[28] J Wang, AN Rider, M Heller, and R Kaye. Theoretical and experimental research into optimal edge taper of bonded repair patches subject to fatigue loadings. *International journal of adhesion and adhesives*, 25(5):410–426, 2005.

[29] M Heller and R Kaye. Shape optimisation for bonded repairs. *Advances in the bonded composite repair of metallic aircraft structure*, pages 269–315p, 2002.

[30] RH Kaye and M Heller. Through-thickness shape optimisation of bonded repairs and lap-joints. *International journal of adhesion and adhesives*, 22(1):7–21, 2002.

[31] S Kumar. Analysis of tubular adhesive joints with a functionally modulus graded bondline subjected to axial loads. *International Journal of Adhesion and Adhesives*, 29(8):785–795, 2009.

[32] S Kumar and JP Scanlan. On axisymmetric adhesive joints with graded interface stiffness. *International Journal of Adhesion and Adhesives*, 41:57–72, 2013.

[33] S Kumar and MA Khan. An elastic solution for adhesive stresses in multi-material cylindrical joints. *International Journal of Adhesion and Adhesives*, 64:142–152, 2016.

[34] Shanmugan Kumar and KL Mittal. *Advances in modeling and design of adhesively bonded systems*. John Wiley & Sons, 2013.

[35] MY Quek and CY Yue. Axisymmetric stress distribution in the single filament pull-out test. *Materials Science and Engineering: A*, 189(1):105–116, 1994.

[36] S Kumar and PC Pandey. Behaviour of bi-adhesive joints. *Journal of Adhesion Science and Technology*, 24(7):1251–1281, 2010.

[37] Lucas FM da Silva and Maria João CQ Lopes. Joint strength optimization by the mixed-adhesive technique. *International Journal of Adhesion and Adhesives*, 29(5):509–514, 2009.

[38] S Kawasaki, G Nakajima, K Haraga, and C Sato. Functionally graded adhesive joints bonded by honeymoon adhesion using two types of second generation acrylic adhesives of two components. *The Journal of Adhesion*, 92(7-9):517–534, 2016.

[39] S Kumar. Modeling of cylindrical joints with a functionally graded adhesive interlayer. In *Advances in Modeling and Design of Adhesively Bonded Systems*, pages 47–91. Scrivener Publishing; Wiley, 2013.

[40] S Kumar and MA Khan. A shear-lag model for functionally graded adhesive anchors. *International Journal of Adhesion and Adhesives*, 68:317–325, 2016.

[41] Lucas FM da Silva, Andreas Öchsner, and Robert D Adams. *Handbook of adhesion technology*. Springer Science & Business Media, 2011.

[42] A Saez, MP Ariza, and J Dominguez. Three-dimensional fracture analysis in transversely isotropic solids. *Engineering analysis with boundary elements*, 20(4):287–298, 1997.

[43] Johannes Liljenhjerte and S Kumar. Pull-out performance of 3d printed composites with embedded fins on the fiber. In *MRS Proceedings*, volume 1800, pages mrss15–2135597. Cambridge Univ Press, 2015.

[44] Johannes Liljenhjerte, Priyank Upadhyaya, and S Kumar. Hyperelastic strain measurements and constitutive parameters identification of 3d printed soft polymers by image processing. *Additive Manufacturing*, 11:40–48, 2016.

8 Tables and Figures

Table 1: Material and geometric properties of crack-patch assembly

Member	Material	$E^{(i)}$ (MPa)	$\nu^{(i)}$	Radius a (mm)	Thickness h_i(mm)
Substrate (1)	Aluminium Alloy	72000	0.30	50	2.0
Adhesive (3)	Epoxy glue	2700	0.35	50	0.1
Patch (2)	Aluminium Alloy	72000	0.30	50	2.0

Table 2: Material properties to demonstrate the effect of stiffness ratio

Assembly	Substrate	Patch	Stiffness ratio ($E^{(3)}/E^{(1)}$)
I	Al ($E^{(1)}$= 70 GPa, $\nu^{(1)}$ = 0.3)	Ti ($E^{(3)}$= 100 GPa, $\nu^{(3)}$ = 0.3)	0.7
II	Al ($E^{(1)}$= 70 GPa, $\nu^{(1)}$ = 0.3)	Al ($E^{(3)}$= 70 GPa, $\nu^{(3)}$ = 0.3)	1
III	Ti ($E^{(1)}$= 100 GPa, $\nu^{(1)}$ = 0.3)	Al ($E^{(3)}$= 70 GPa, $\nu^{(3)}$ = 0.3)	1.43

Table 3: Material used to implement composite adherends [42]

Material	Properties	Remark
A	Al (E= 70 GPa, ν = 0.3)	Isotropic
B	Composite ($E_r = E_\theta$ = 10 GPa, E_z = 20 GPa, $\nu_r = \nu_\theta = \nu_{r\theta}$ = 0.3, ν_{rz} = 0.15)	Transverely Isotropic

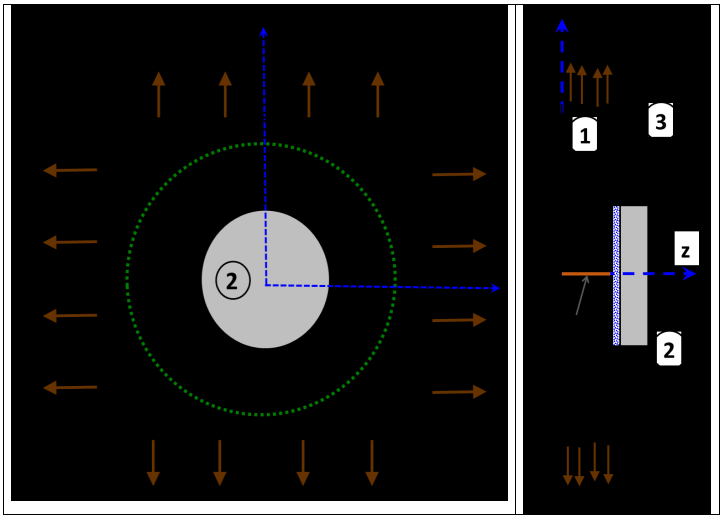

Figure 1: Substrate with a through-thickness hairline defect is repaired using an adhesively bonded patch. Region (1) represents the substrate, region (2) represents patch and region (3) represents the adhesive interlayer.

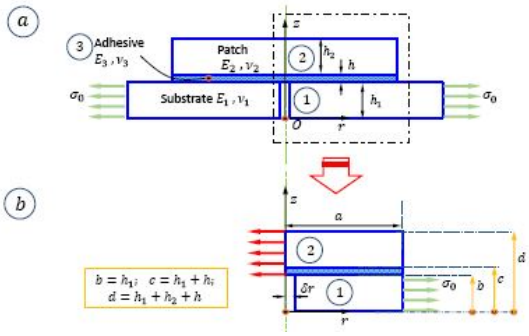

Figure 2: Crack-patch 3D axisymmetric assembly subjected to a far-field stress σ_0

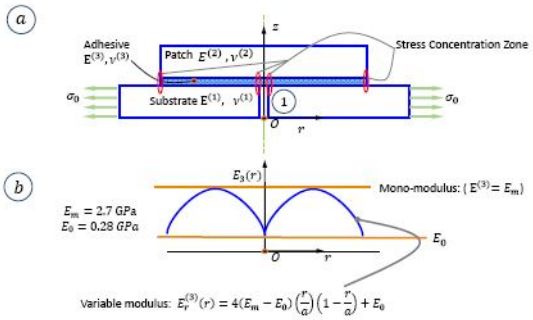

Figure 3: Homogeneous and Graded bondline adhesive: a) Geometric model with stress concentration zones. b) Variation of modulus over the bond radius

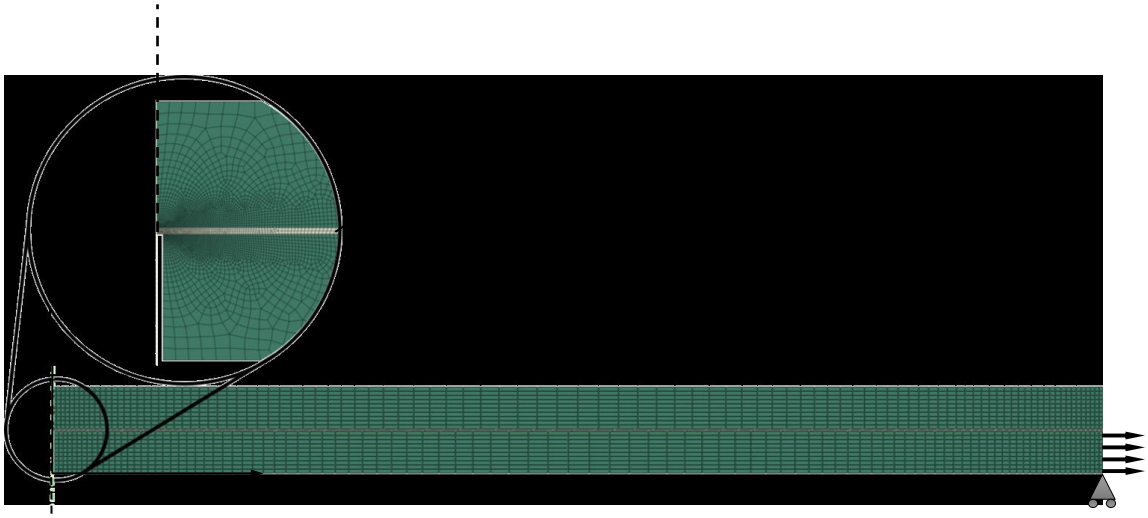

Figure 4: Finite element mesh for axisymmetric crack-patch assembly

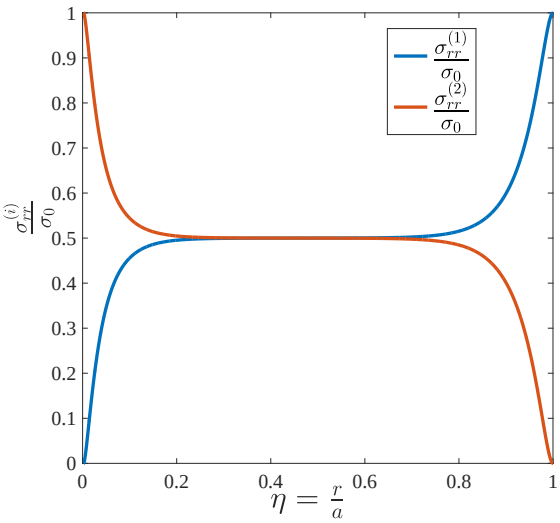

Figure 5: MMB: Radial stresses in the adherends over the bondline for σ_0 = 100 MPa; $\sigma_{rr}^{(1)}$ is the primary unknown function in the model.

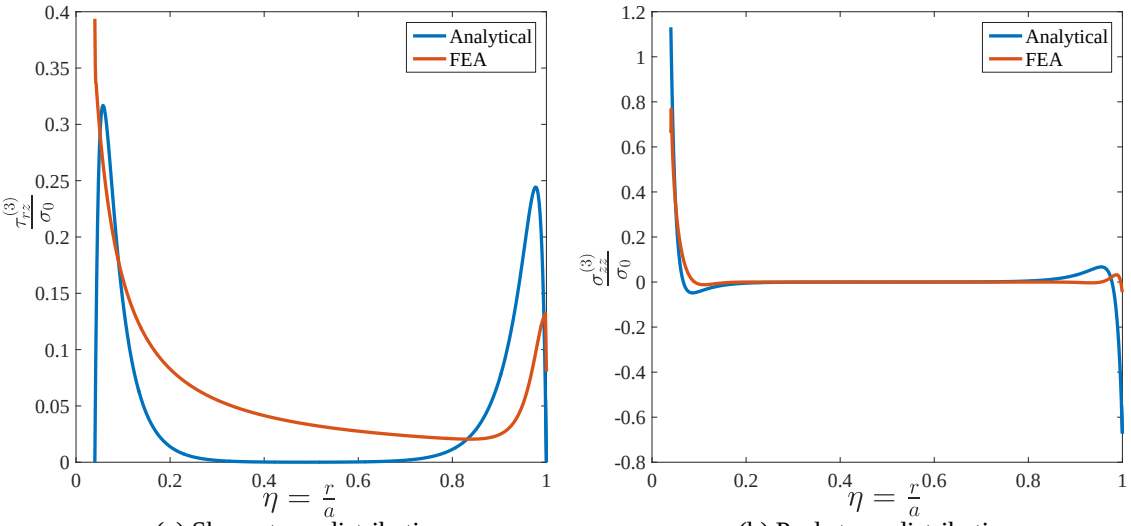

(a) Shear stress distribution

(b) Peel stress distribution

Figure 6: MMB (Analytical vs FEA): Comparison of shear and peel stress distribution at the mid-surface of interlayer along the bond radius obtained from analytical model with an analogous FE model for σ_0 = 100 MPa, a = 50 mm and δr = 2 mm

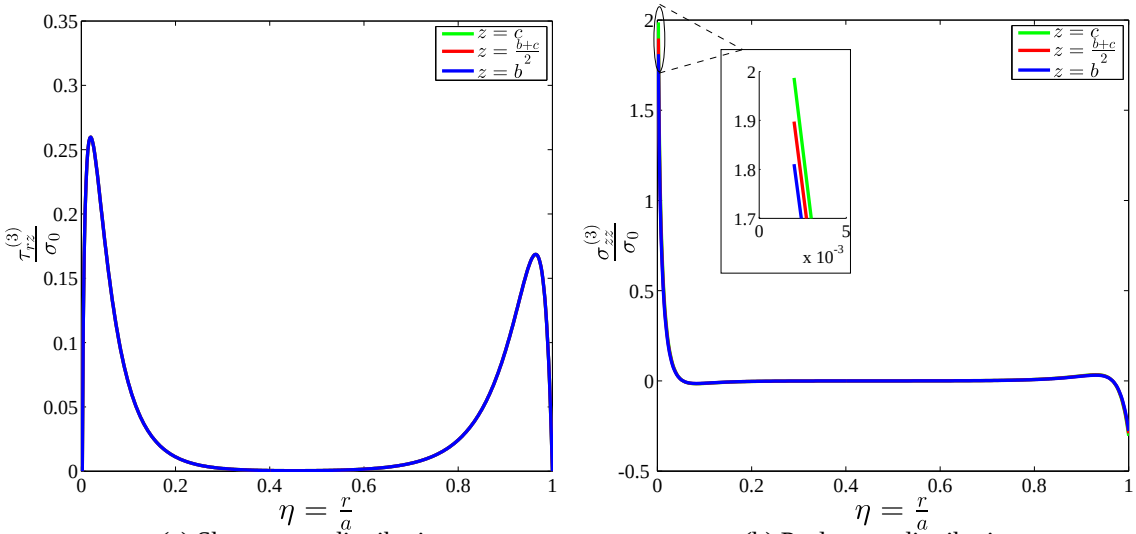

(a) Shear stress distribution (b) Peel stress distribution

Figure 7: MMB: Stress distribution at critical surfaces along the bond radius for σ_0 = 100 MPa

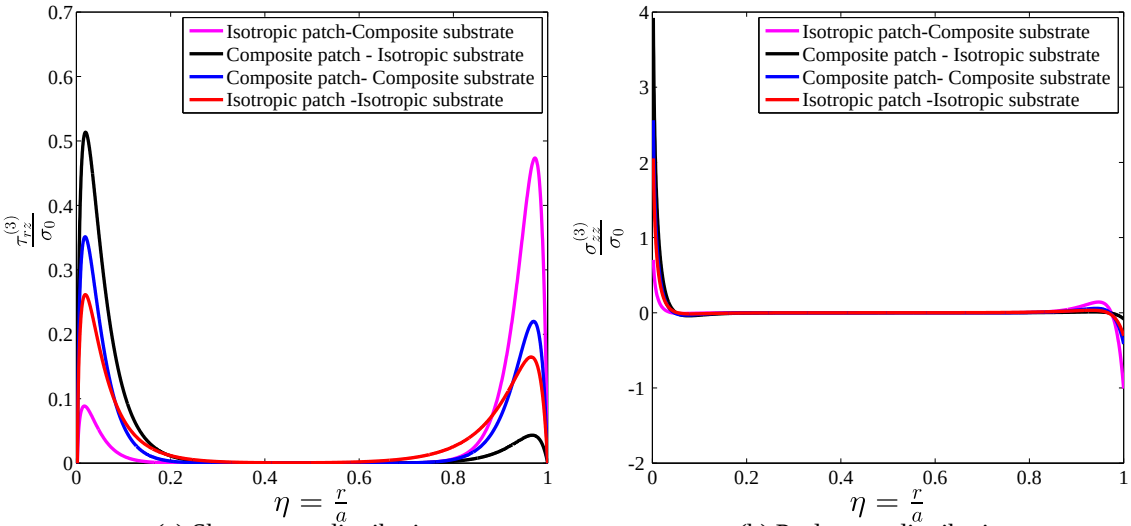

(a) Shear stress distribution (b) Peel stress distribution

Figure 8: MMB: Peak shear and peel stresses at the mid-surface of the adhesive for composite adherends for σ_0 = 100 MPa

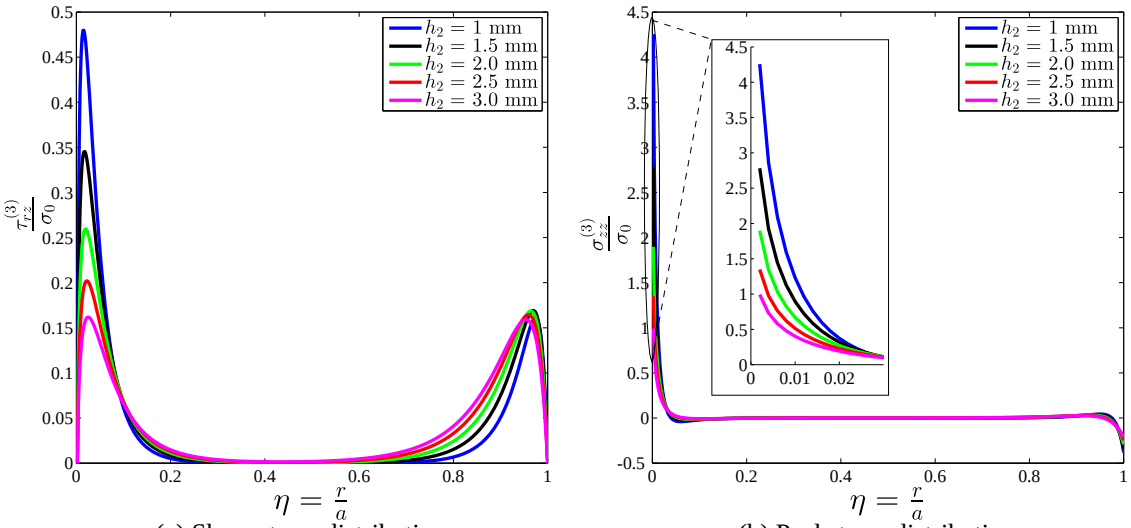

(a) Shear stress distribution

(b) Peel stress distribution

Figure 9: MMB: Stress distribution at the mid-surface of the adhesive as a function of patch thickness h_2 over the bond radius for σ_0 = 100 MPa

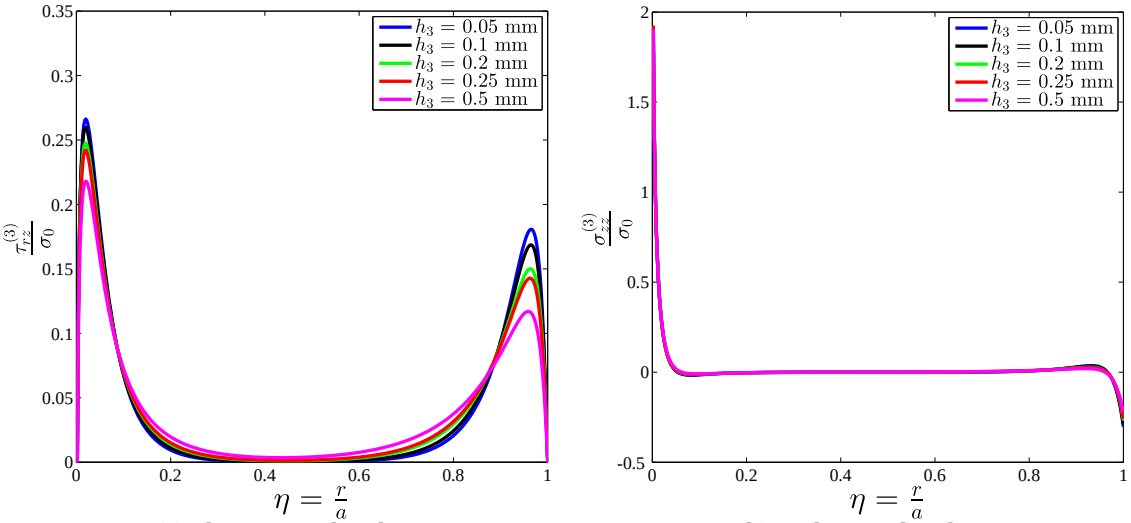

(a) Shear stress distribution (b) Peel stress distribution

Figure 10: MMB: Stress distribution at the mid-surface of the adhesive as a function of adhesive thickness h_3 over the bond radius for σ_0 = 100 MPa

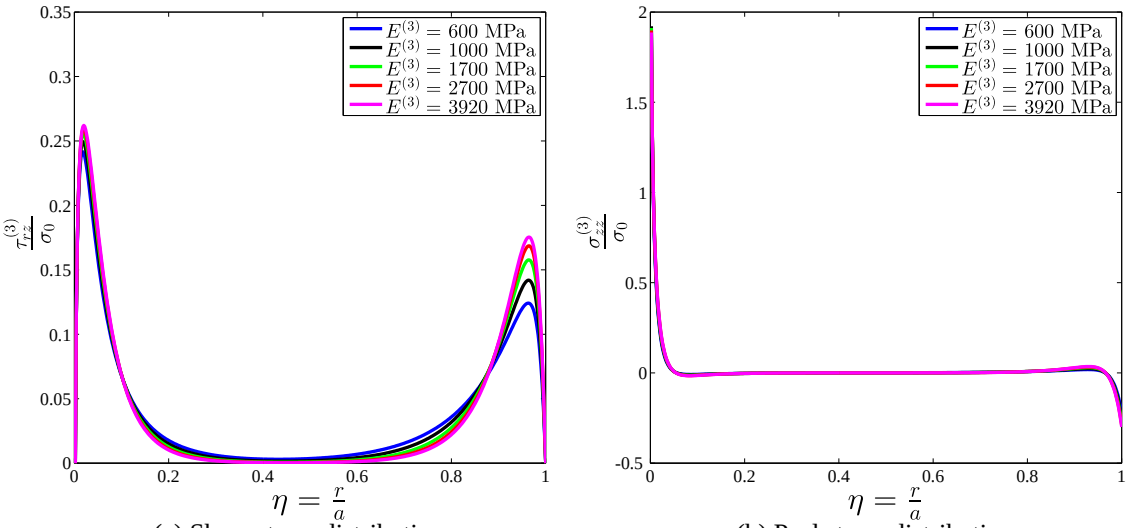

(a) Shear stress distribution (b) Peel stress distribution

Figure 11: MMB: Stress distribution at the mid-surface of the adhesive as a function of adhesive's modulus $E^{(3)}$ over the bond radius for σ_0 = 100 MPa

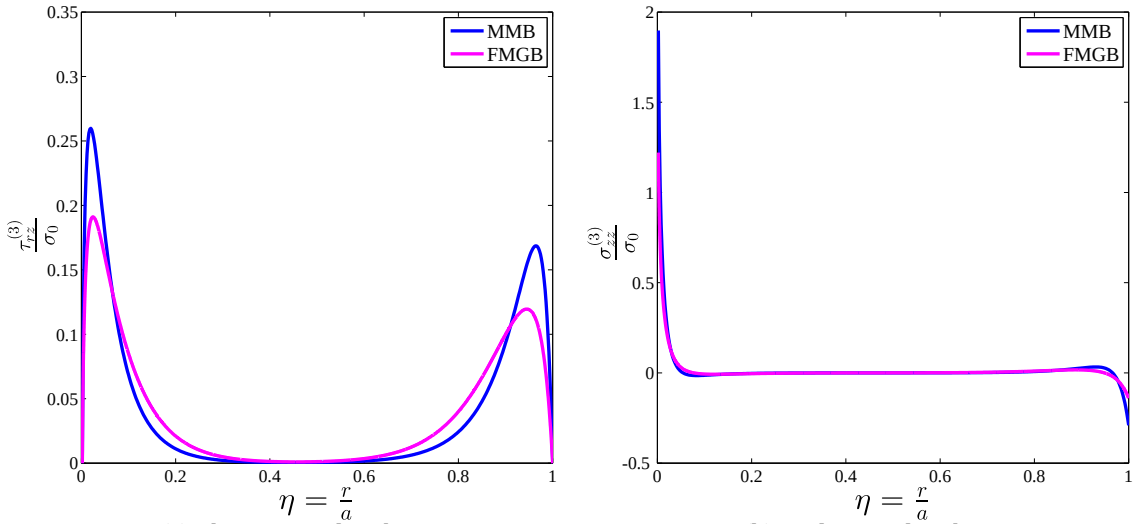

(a) Shear stress distribution (b) Peel stress distribution

Figure 12: MMB Vs FMGB: Stress distribution in the adhesive at the mid-surface of the adhesive $\left(z = \frac{b+c}{2}\right)$ over the bond radius for $\sigma_0 = 100$ MPa

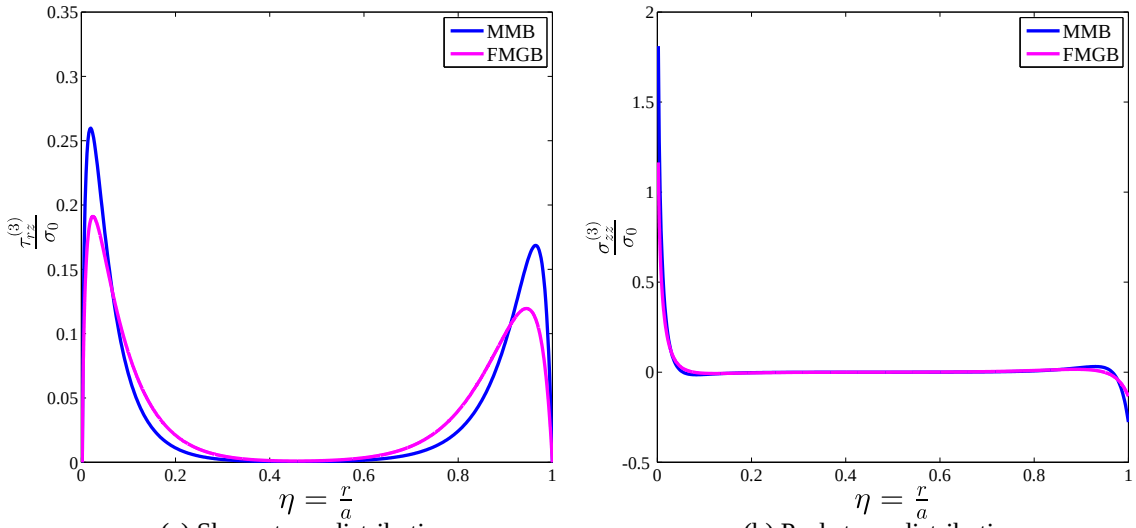

(a) Shear stress distribution (b) Peel stress distribution

Figure 13: MMB Vs FMGB: Stress distribution in the adhesive at the interface of substrate and adhesive ($z = b$) over the bond radius for $\sigma_0 = 100$ MPa

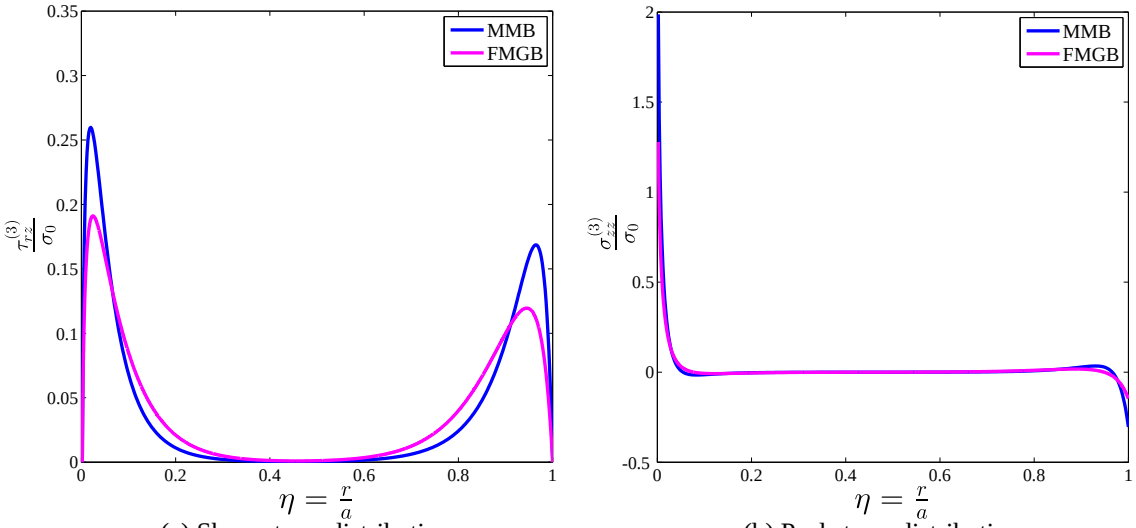

(a) Shear stress distribution (b) Peel stress distribution

Figure 14: MMB Vs FMGB: Stress distribution in the adhesive at the interface of adhesive and patch ($z = c$) over the bond radius for $\sigma_0 = 100$ MPa

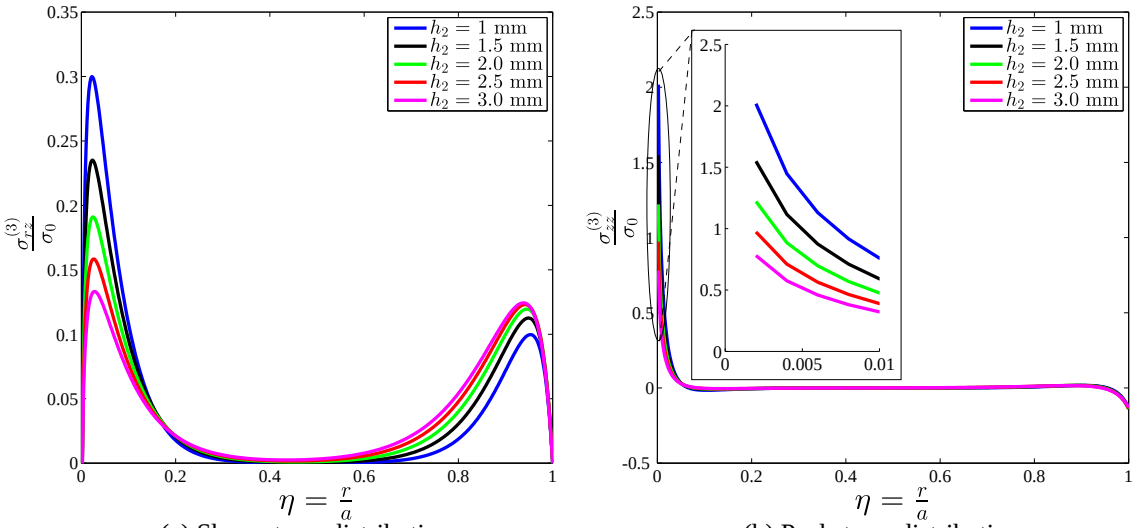

(a) Shear stress distribution

(b) Peel stress distribution

Figure 15: FMGB: Stress distribution at the mid-surface of the adhesive as a function of patch thickness h_2 over the bond radius for $\sigma_0 = 100$ MPa

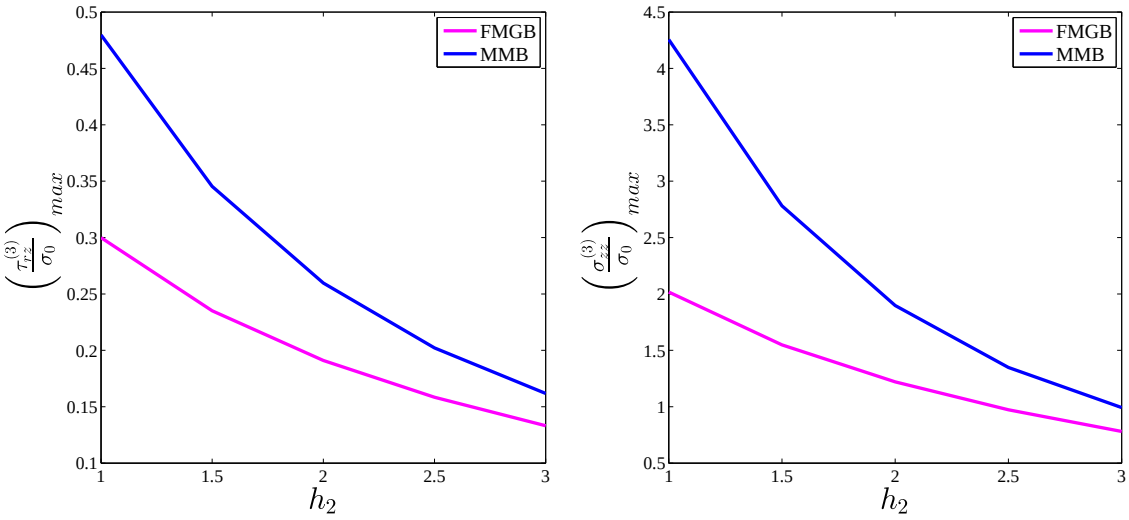

(a) Peak shear stress Vs patch thickness h_2 (b) Peak peel stress Vs patch thickness h_2

Figure 16: MMB Vs FMGB: Peak shear and peel stresses at the mid-surface of the adhesive for varying patch thicknesses for σ_0 = 100 MPa

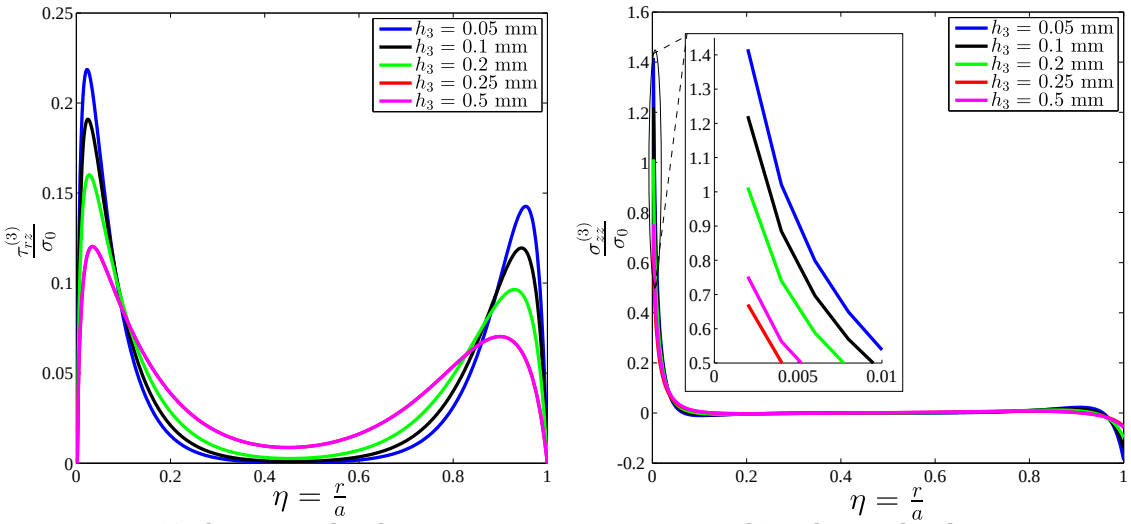

(a) Shear stress distribution

(b) Peel stress distribution

Figure 17: FMGB: Stress distribution at the mid-surface of the adhesive as a function of adhesive thickness h_3 over the bond radius for $\sigma_0 = 100$ MPa

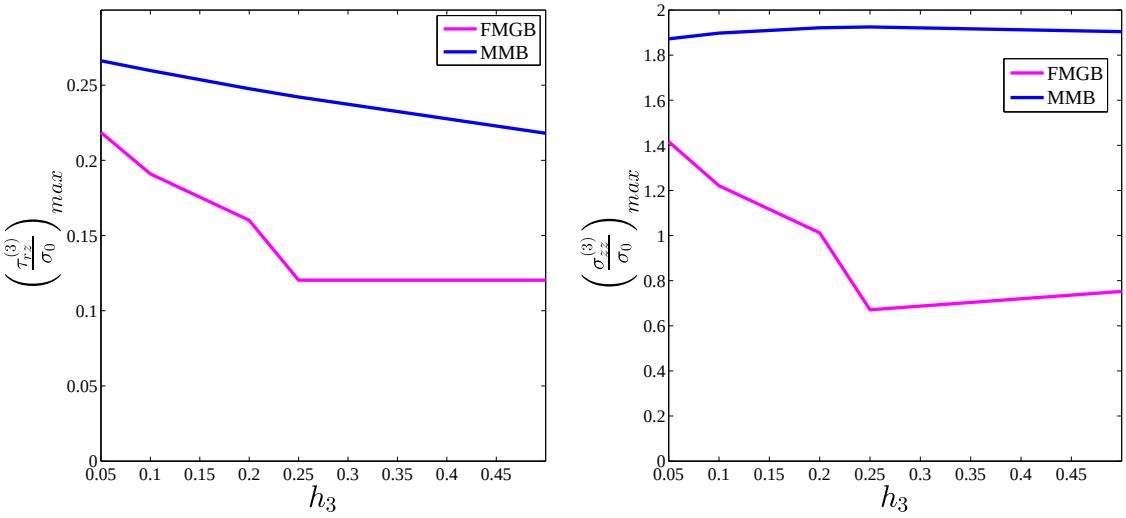

(a) Peak shear stress Vs adhesive thickness h_3 (b) Peak peel stress Vs adhesive thickness h_3

Figure 18: MMB Vs FMGB: Peak shear and peel stresses at the mid-surface of the adhesive for varying adhesive thicknesses for σ_0 = 100 MPa

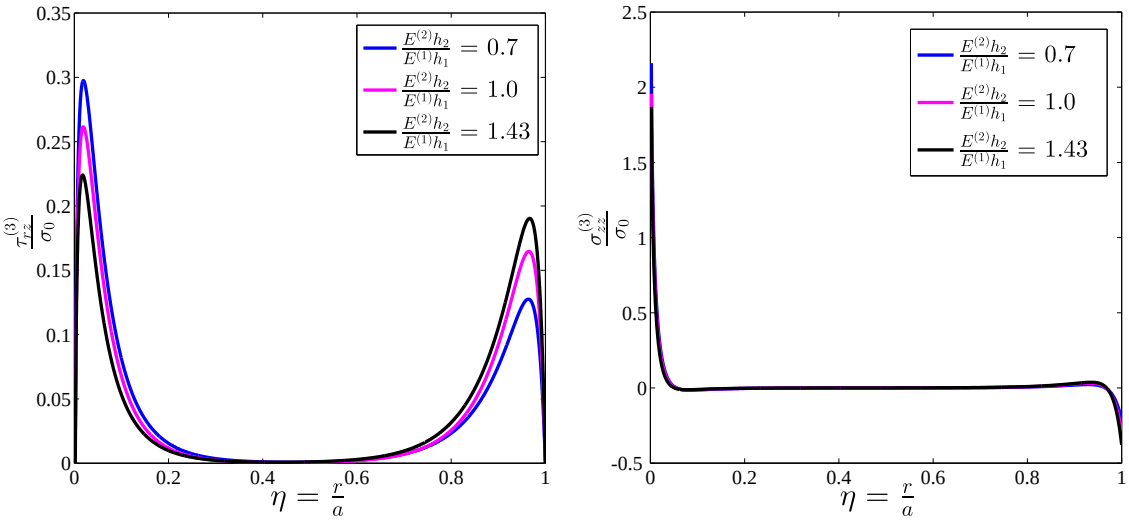

(a) Shear stress distribution (b) Peel stress distribution

Figure 19: MMB: Peak shear and peel stresses at the mid-surface of the adhesive for varying stiffness ratios for σ_0 = 100 MPa